JOURNAL OF PROPULSION AND POWER
Vol. 23, No. 2, March–April 2007

Analytical Approach for Investigating Bristle/Backplate Hysteresis Phenomenon in Brush Seals

Haifang Zhao* and Robert J. Stango†
Marquette University, Milwaukee, Wisconsin 53233

DOI: 10.2514/1.20682

Brush seals are an important innovation, increasing the efficiency of turbomachinery for both land-based and aeronautical applications. However, a performance drawback termed *brush seal hysteresis* has been reported that can promote seal leakage, thereby undermining the effectiveness of the brush seal system. It is generally recognized that hysteretic behavior may be attributed to complex frictional forces that are generated within the brush seal during service, and that appropriate steps must be undertaken to understand, quantify, and minimize this source of inefficiency in brush seal performance. This paper focuses on investigating hysteresis phenomenon that can be traced to a mechanical interaction between the bristle and back plate of the brush seal. To this end, a mechanics-based model is developed that can forecast both bristle deformation and friction forces that arise between the lateral surface of the bristle and the edge of the back plate. The model uses general bending theory to examine three-dimensional deformation of the fiber that is caused by transient, flow-induced axial loads within the jet engine. Correctness of solutions obtained from the model is validated by a direct comparison with known results that have been published in the literature. On the basis of the mechanics model, a friction force path-based approach is proposed for quantifying brush seal hysteresis, and results are presented indicating that the model can successfully forecast a stick-slip phenomenon that naturally arises due to the axial flow of gases through the annular interspace between the rotor and brush seal back plate.

Nomenclature

A	=	bristle cross-sectional area
b	=	fiber length on the back plate
C	=	torsion rigidity
D_f	=	brush seal diameter measured between undeformed bristle tips
D_s	=	rotor diameter
E	=	bristle modulus of elasticity
EI	=	bristle modulus of rigidity
F_N	=	contact force between the fiber and back plate edge
F_{NX}, F_{NY}, F_{NZ}	=	component of F_N along the global X_o, Y_o, and Z_o direction, respectively
F_{nx}, F_{ny}, F_{nz}	=	components of F_N along local x, y, and z axes, respectively
f	=	friction force between the fiber and the back plate edge
G^*	=	radial design separation (i.e., gap) between rotor surface and seal back plate
G, G'	=	components of the internal bending moments on fiber cross section S in the x and y direction, respectively
H	=	torsion couple in the fiber
H^*	=	bristle length along radial direction
I	=	bristle moment of inertia
$\boldsymbol{i}$, $\boldsymbol{j}$, $\boldsymbol{k}$	=	unit vector along the local coordinate axes x, y, and z, respectively
L	=	bristle length
$\bar{L}$	=	dimensionless bristle length over the back plate $\bar{L} = b/L$
l_i, m_i, n_i	=	direction cosines of the local x, y, and z axes with respect to the fixed X_o, Y_o, Z_o
N, N'	=	components of the shear force at an arbitrary wire cross section in the x, y direction, respectively
$\boldsymbol{n}_1$	=	unit vector that is tangent to the back plate edge at the fiber/back plate contact point
$\boldsymbol{n}_2$	=	unit vector that is tangent to the deformed fiber at the fiber/back plate contact point
P	=	axial flow-induced concentrated load
$\bar{P}$	=	dimensionless axial flow-induced concentrated load $\bar{P} = PL^2/EI$
R_s	=	rotor radius
r	=	bristle radius
S	=	arbitrary cross section of fiber
s	=	arc length coordinate along bristle neutral axis
s_1	=	arc length measured form the fixed end of the fiber until the fiber/back plate contact point
s^*	=	dimensionless arc length coordinate along bristle neutral axis
T	=	axial tension in the fiber
u, v	=	bristle deflection in x and y direction, respectively
$\bar{u}$, $\bar{v}$	=	dimensionless bristle deflection in x and y direction, respectively, $\bar{u} = u/L$, $\bar{v} = v/L$
W_{fu}, W_{fd}	=	work that friction force did during uploading and downloading, respectively
W_{pu}, W_{pd}	=	work that force P did during uploading and downloading, respectively
y	=	direction coordinate perpendicular to axis along undeformed bristle
y_{ξ_2}	=	y coordinate of bristle contact point along the back plate edge coordinate ξ_2
z	=	direction coordinate along undeformed bristle
$\bar{z}$	=	dimensionless coordinate along z axis
z_{ξ_2}	=	z coordinate of bristle contact point along the back plate edge coordinate ξ_2

Presented as Paper 3983 at the 41st AIAA/ASME/SAE/ASEE Joint Propulsion Conference & Exhibit, Tucson Arizona, 10–13 July 2005; received 21 October 2005; revision received 29 March 2006; accepted for publication 4 April 2006.

*Graduate Research Assistant, Department of Mechanical Engineering. Student Member AIAA.

†Professor of Mechanical Engineering, Department of Mechanical Engineering; robert.stango@marquette.edu. Member AIAA (corresponding author).

β	=	angle relating tangent direction of the back plate edge to the fixed coordinate axes Y_0, Z_0
Δ_o^*	=	initial uniform radial interference between rotor diameter and undeformed brush seal diameter
ΔE	=	energy change
ΔW_f	=	differential work that friction force did during the load cycle
ΔW_p	=	differential work that load P did during the load cycle
ε	=	solution convergence parameter
θ	=	bristle lay angle
κ, κ', τ	=	components of vector $\boldsymbol{\omega}$ along local x, y, and z directions, defined as the components of curvature κ, κ' and the twist per unit length τ, respectively
μ_s	=	static friction coefficient
μ_k	=	kinetic friction coefficient
ν	=	Poisson's ratio
ξ_2	=	back plate edge coordinate along circumferential direction
ϕ	=	local slope at coordinate position s on deflected bristle
$\boldsymbol{\omega}$	=	constant angular velocity vector

I. Introduction

BRUSH seals have proven to be an effective replacement for labyrinth seals in turbomachinery applications. Experience has shown that a significant reduction in secondary leakage flows can be obtained when the brush seal is designed and properly applied in the application. However, due to the complex loading that a brush seal is subjected to during service, a complete understanding of brush seal behavior is not yet available.

As shown in Figs. 1a and 1b, a brush seal consists of an ordered array of densely packed fine wires that are secured between a front and back plate. The seal itself resides between successive stages of the turbine whereupon air is compressed by turbine blades that are attached to the rotating shaft. Thus, the brush seal provides a fibrous barrier against leakage, as gases attempt to move toward the downstream region of the turbine. In Fig. 1b (see inset) the oncoming flow of gas is shown in the vicinity of the face of the brush seal, and leakage is depicted as the movement of gas through the constricted space G^* between the seal back plate and shaft surface.

The flow/leakage of gas through the brush seal is very complex and has been examined using both theoretical and experimental methods of analysis. Generally, the brush seal is modeled as a series of cantilever beams that are subjected to forces that can vary both along the bristle length, and the through-thickness direction of the seal. Consider, for example, the vertical section lines a–a, b–b, and c–c shown in the inset of Fig. 1b. At the entrance of the seal face (section line a–a), a radially inward fluid flow termed "blowdown" has been examined by several researchers, including Bayley and Long [1], Wood [2], and Chen et al. [3]. Also, as reported by Zhao and Stango [4], the radially inward flow of gas can give rise to increased contact forces at the interface of the bristle tip and shaft surface. Within the central portion of the seal (section line b–b), tightly packed fibers are subjected to the oncoming flow of gases that can lead to compaction of the bristle network. However, at the extreme right position of the brush seal (section line c–c), bristles are supported and constrained by the back plate, which offers resistance to bristle bending as gases move rapidly through the rotor/seal interface G^*. Finally, bristle tips that are positioned along horizontal section line d–d, can be subjected to radial excursions caused by rotor/bristle design interference, rotor eccentricity, and dimensional changes that are associated with thermomechanical loads applied to the system. Also, filament tips are subjected to a circumferential load that arises as a consequence of rotor-induced swirl.

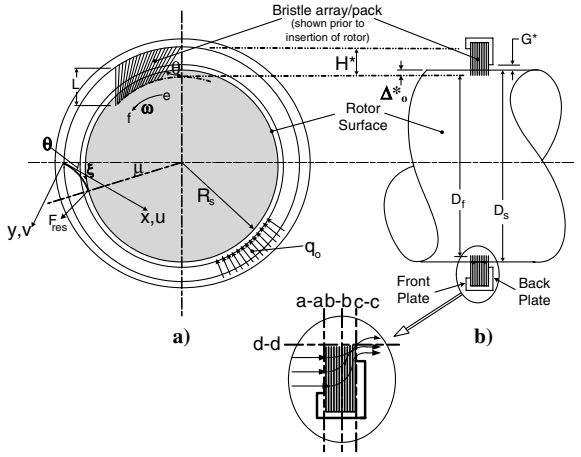

Fig. 1 a) Downstream view of brush seal. b) Section view of annular front and back plate that constrain bristle pack; arrows (inset) depict complex fluid flow.

This paper is aimed at examining bristle deformation that occurs along c–c, that is, in the immediate vicinity of the back plate of the brush seal. The problem derives its importance from the fact that, during service, bristles along the back plate are subjected to transient loads, which result in the displacement of the fibers from their equilibrium positions. However, due to friction forces that exist between the neighboring bristles and back plate, the deformed bristles cannot fully recover from their deflected shape, and therefore, can remain locked in position when transient loads are diminished. As a result, leakage can increase considerably when compared with acceptable levels that are associated with nominal design interference for a concentrically rotating shaft. Although this "bristle lock" and change in brush seal performance has been termed "hysteresis," the phenomenon has yet to be quantified and systematically investigated as an inherent property of brush seal systems. Therefore, this paper is also aimed at developing a mechanics-based rationale for computing bristle/backplate hysteresis, thereby providing a basis for understanding important relationships among brush seal tribology, performance, and design.

The hysteresis phenomenon has been observed by many experimental researchers. In 1993, Chupp and Dowler [5] found that, during brush seal performance tests, leakage performance under a given pressure ratio depends on whether this pressure ratio is reached by an increase or decrease in the pressure. Studies conducted by Basu et al. [6] have indicated that an axial pressure differential across the brush seal intensifies frictional forces between neighboring bristles and at the back plate. As a result, any subsequent radial movement of the shaft can alter the effectiveness of the brush seal.

In an effort to obtain an improved understanding of brush seal hysteresis behavior, previous researchers have proposed several approaches for simulating this phenomenon. Aksit and Tichy [7], for example, have used a discretization technique for computing bristle force and deformation. Their model consisted of a representative bristle bundle rubbing against a rigid backplate surface. Each bristle was discretized using 3-D quadratic beam elements, and various contact elements were used to simulate bristle/rotor contact, interbristle contact, and bristle/back plate contact, respectively. Using Coulomb's law of friction as a basis for computing frictional contact forces, their findings indicated that the model can be used to forecast bristle hysteresis. Howell and Lattimer [8] have proposed a single bristle bending model to simulate the locking phenomenon of a bristle located adjacent to the backplate. In this model, deformation of a single bristle is computed under the action of an assumed concentrated load (axial flow load) applied at the fiber tip using linear beam theory. Although the effect of frictional interaction between the bristle and the back plate is included in their model, the authors note that for a range of practical coefficients of friction, locking of a single bristle cannot be predicted on the basis of small deformation (i.e., linear) beam theory. Therefore, an alternate model is needed to evaluate the brush seal hysteresis phenomenon. The role of *distributed interbristle* friction force on brush seal hysteresis has been reported by Zhao and Stango [9]. Their model has demonstrated

that the combination of interbristle friction force and compaction of the bristle pack due to axial fluid flow can result in a uniformly distributed internal micromoment that resists bending deformation. Consequently, interbristle friction force can give rise to a delayed filament displacement as well as an incomplete bending recovery of bristles. As a result, a gap can form between the rotor and bristle tips, which inevitably increase the flow of leakage.

In this paper, a mechanics-based model is developed for evaluating the deflection of a single bristle that is subjected to an out-of-plane transverse load at the tip of the filament. Thus, as in previously reported research, a concentrated end load is used for approximating the total axial flow force that arises as gases rapidly move through the shaft/seal interface. General bending theory is applied to compute bristle out-of-plane deformation and the solutions obtained herein are validated by a direct comparison with results reported by Howell and Lattimer [8]. The present work clearly indicates that as the single bristle deforms, sliding motion occurs between the side of the fiber and the edge of the back plate. Thus, hysteresis is defined and computed on the basis of the work done by the frictional force that acts along the interface of the bristle and back plate edge. A closed hysteresis loop is thus identified and defined as the path-dependent area that is generated when the transverse load undergoes one complete uploading/downloading cycle. Two case studies for hysteresis are reported, namely, $\mu_s = \mu_k$ and $\mu_s > \mu_k$ for a range of friction coefficients. It is shown that the severity of hysteresis phenomenon is dependent upon not only the magnitude of the friction coefficient, but also the relative magnitude of the static and kinetic friction coefficient.

II. Theoretical Background and Formulation of Problem

The current problem is depicted in Fig. 2a, whereby a single bristle taken from the last row of the bristle array is isolated and examined. The undeflected bristle having length L is oriented at the fiber lay angle θ. Also shown is a concentrated load of arbitrary magnitude P (force), which arises due to the axial fluid flow passing through the bristle network along the annular region G^* [see Fig. 1b]. Because this region generally is only 10% of the whole bristle length, one may approximate the distributed transverse fluid load as a concentrated load applied at the fiber tip. Also, CFD calculations [10] have shown that the velocity of airflow is greatest near the fiber tip. Friction force f between the fiber and the back plate is shown in Figs. 2a and 2b, and is directed along coordinate ξ_2, that is, tangent to the back plate edge, as illustrated in Fig. 2b. The magnitude of f is presumed to obey Coulomb's law of friction.

Although a planar view of bristle deformation is depicted in Fig. 2c, it is apparent that a nonzero lay angle θ gives rise to three-dimensional bristle deformation under the action of load P, that is, the fiber not only bends along the direction of force P, but also deforms along the direction of back plate edge coordinate ξ_2. As a result, formulation of the problem will be based upon general bending theory for computing the bristle deformation.

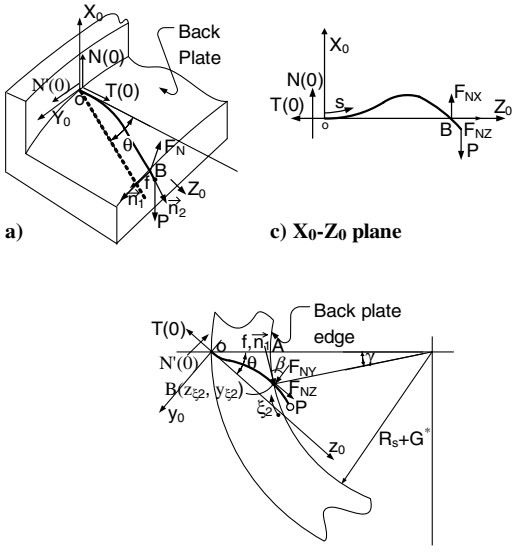

Fig. 2 a) Bristle bending along the back plate edge at point *B*; b) top view of the deformed fiber (Y_0–Z_0 plane view); c) side view of the deformed fiber (X_0–Z_0 plane view).

A. Governing Equations

As shown in Fig. 3, a deformed fiber having internal forces and moments at an arbitrary cross section S is depicted. Coordinate position of the bristle is specified by global coordinates X_0, Y_0, Z_0 and local axes x, y, z, which are principle torsion–flexure axes at an arbitrary point of the deformed fiber [11].

In agreement with customary nomenclature, we suppose the origin of the local coordinate system x, y, z moves with a unit velocity along the deformed neutral axis of the fiber, and the local rotating frame possesses an angular velocity vector $\boldsymbol{\omega}$ at each point along the deformed fiber. Thus, $\boldsymbol{\omega}$ is resolved into three components directed along x, y, and z directions, which are defined as the components of curvature κ, κ' and the twist per unit length τ, respectively.

To a second order of approximation, the equilibrium equations for the deformed fiber can be expressed as follows:

$$\frac{\mathrm{d}N}{\mathrm{d}s} - N'\tau + T\kappa' = 0 \tag{1}$$

$$\frac{\mathrm{d}N'}{\mathrm{d}s} - T\kappa + N\tau = 0 \tag{2}$$

$$\frac{\mathrm{d}T}{\mathrm{d}s} - N\kappa' + N'\kappa = 0 \tag{3}$$

$$\frac{\mathrm{d}G}{\mathrm{d}s} - G'\tau + H\kappa' - N' = 0 \tag{4}$$

$$\frac{\mathrm{d}G'}{\mathrm{d}s} + G\tau - H\kappa + N = 0 \tag{5}$$

$$\frac{\mathrm{d}H}{\mathrm{d}s} - G\kappa' + G'\kappa = 0 \tag{6}$$

the above six differential equilibrium equations contain nine unknown quantities, namely N, N', T, G, G', H, κ, κ', and τ. Thus, three additional equations are required to determine the deformation (curvature and twist) of the fiber. In addition, the relationship between internal moments, curvature, torque, and twist are based upon the familiar "Bernoulli–Euler" relations:

$$G = EI_x\kappa \tag{7a}$$

$$G' = EI_y\kappa' \tag{7b}$$

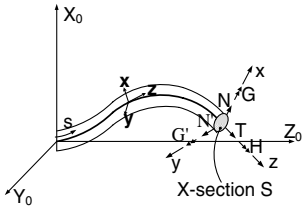

Fig. 3 Internal loads within an arbitrary fiber.

$$H = C\tau \tag{7c}$$

If the fiber cross section is circular with radius r, then

$$I_x = I_y = I = \frac{\pi r^4}{4} \tag{8}$$

$$C = \frac{\pi r^4}{4(1+\nu)} \tag{9}$$

where ν is Possion's ratio.

Substituting Eqs. (7a–7c) into Eqs. (4–6), one obtains

$$EI\frac{\mathrm{d}\kappa}{\mathrm{d}s} - EI\kappa'\tau + C\tau\kappa' - N' = 0 \tag{10}$$

$$EI\frac{\mathrm{d}\kappa'}{\mathrm{d}s} - C\tau\kappa + EI\kappa\tau + N = 0 \tag{11}$$

$$C\frac{\mathrm{d}\tau}{\mathrm{d}s} = 0 \tag{12}$$

However, because $C \neq 0$, we require

$$\frac{\mathrm{d}\tau}{\mathrm{d}s} = 0 \tag{13}$$

and conclude

$$\tau(s) = \text{const} \tag{14}$$

Moreover, because no twisting moment H exists at the fiber tip ($s = L$), that is, $H|_{s=L} = 0$, then Eq. (7c) yields

$$\tau|_{s=L} = 0 \tag{15}$$

Together, Eqs. (14) and (15) yield the following:

$$\tau(s) = \text{const} = 0 \tag{16}$$

Final form of the governing equilibrium equations is obtained by inserting Eq. (16) into Eq. (10) and (11) and Eqs. (1–3):

$$EI\frac{\mathrm{d}\kappa}{\mathrm{d}s} - N' = 0 \tag{17}$$

$$EI\frac{\mathrm{d}\kappa'}{\mathrm{d}s} + N = 0 \tag{18}$$

$$\frac{\mathrm{d}N}{\mathrm{d}s} + T\kappa' = 0 \tag{19}$$

$$\frac{\mathrm{d}N'}{\mathrm{d}s} - T\kappa = 0 \tag{20}$$

$$\frac{\mathrm{d}T}{\mathrm{d}s} - N\kappa' + N'\kappa = 0 \tag{21}$$

Summarizing, the current problem consists of the above five equilibrium equations along with five unknowns, N, N', T, κ, and κ'.

Table 1 Cosine directions of local x, y, z axes with respect to fixed X_0, Y_0, Z_0 axes

	X_0	Y_0	Z_0
x	l_1	m_1	n_1
y	l_2	m_2	n_2
z	l_3	m_3	n_3

B. Coordinate System Transformation and Direction of Contact Force F_N

1. Coordinate System Transformation

The local coordinate system x, y, and z is related to the fixed axes X_0, Y_0, Z_0 by the scheme in Table 1 [11] where, for example, l_1, m_1, n_1 are the direction cosines with respect to the global axes for the x axis. Similar definitions are applicable for the y and z axes.

For the current problem, one can readily demonstrate that the relations among direction cosines and curvature are given by

$$\frac{\mathrm{d}l_1}{\mathrm{d}s} = -l_3\kappa' \tag{22}$$

$$\frac{\mathrm{d}m_1}{\mathrm{d}s} = -m_3\kappa' \tag{23}$$

$$\frac{\mathrm{d}N_1}{\mathrm{d}s} = -n_3\kappa' \tag{24}$$

$$\frac{\mathrm{d}l_2}{\mathrm{d}s} = l_3\kappa \tag{25}$$

$$\frac{\mathrm{d}m_2}{\mathrm{d}s} = m_3\kappa \tag{26}$$

$$\frac{\mathrm{d}N_2}{\mathrm{d}s} = n_3\kappa \tag{27}$$

$$\frac{\mathrm{d}l_3}{\mathrm{d}s} = l_1\kappa' - l_2\kappa \tag{28}$$

$$\frac{\mathrm{d}m_3}{\mathrm{d}s} = m_1\kappa' - m_2\kappa \tag{29}$$

$$\frac{\mathrm{d}N_3}{\mathrm{d}s} = n_1\kappa' - n_2\kappa \tag{30}$$

If we take the global coordinate axis to coincide with the local coordinate axes at $s = 0$, the following initial conditions are obtained:

$$\begin{gathered} l_1|_{s=0} = 1; \qquad m_2|_{s=0} = 1; \qquad n_3|_{s=0} = 1 \\ l_2|_{s=0} = l_3|_{s=0} = m_1|_{s=0} = m_3|_{s=0} = n_1|_{s=0} = n_2|_{s=0} = 0 \end{gathered} \tag{31}$$

Thus, the displacement of the deformed fiber with respect to global coordinate can be computed as

$$X(s) = \int_0^s l_3\,\mathrm{d}s \tag{32}$$

$$Y(s) = \int_0^s m_3 \, \mathrm{d}s \tag{33}$$

$$Z(s) = \int_0^s n_3 \, \mathrm{d}s \tag{34}$$

2. Direction of Reaction Force F_N

As shown in Fig. 2a, P is the equivalent concentrated load due to axial fluid flow, $N(0), T(0), N'(0)$ are reaction forces at the fixed end of the fiber ($s = 0$), and F_N is the normal contact force between the back plate edge and the fiber at point B where $s = s_1$. The *magnitude* of F_N is unknown and must be determined as an integral part of the solution. However, the *direction* of F_N can be determined by assuming that the fiber contacts the back plate edge at point B (refer to Fig. 2a). Next, two vectors $\boldsymbol{n}_1$ and $\boldsymbol{n}_2$ are defined as follows: $\boldsymbol{n}_1$ is a unit vector that is tangent to the back plate edge at point B, $\boldsymbol{n}_2$ is a unit vector that is tangent to the deformed fiber at point B, that is, along local coordinate axis z at point B. Because the direction of normal contact force F_N must be perpendicular to both the tangent line of the deformed bristle and the back plate edge at the contact point, then the direction of F_N can be computed as follows:

$$\boldsymbol{F}_N = \boldsymbol{n}_1 \times \boldsymbol{n}_2 \tag{35a}$$

where, as one may observe in Fig. 2b,

$$\boldsymbol{n}_1 = (0, \cos\beta, \sin\beta) \tag{35b}$$

$$\boldsymbol{n}_2 = [l_3(s_1), m_3(s_1), n_3(s_1)] \tag{35c}$$

$$\beta = \theta + \gamma \tag{35d}$$

where s_1 is the arc length measured from the fixed end to the contact point B, $l_3(s_1)$, $m_3(s_1)$, and $n_3(s_1)$ are cosine directions of vector $\boldsymbol{n}_2$ at point B with respect to the global coordinate axes X_0, Y_0, and Z_0, and Z_{ξ_2}, Y_{ξ_2} are global coordinates of point B, as further discussed in the next section. Consequently, the cross product of $\boldsymbol{n}_1$ and $\boldsymbol{n}_2$ is

$$\boldsymbol{n}_1 \times \boldsymbol{n}_2 = \begin{vmatrix} \boldsymbol{i} & \boldsymbol{j} & \boldsymbol{k} \\ 0 & \cos\beta & \sin\beta \\ l_3 & m_3 & n_3 \end{vmatrix} = (n_3\cos\beta - m_3\sin\beta)\boldsymbol{i} + (l_3\sin\beta)\boldsymbol{j} + (-l_3\cos\beta)\boldsymbol{k} \tag{36}$$

and the components of the unit normal vector of F_N can be expressed as

$$\left(\frac{n_3\cos\beta - m_3\sin\beta}{\sqrt{(n_3\cos\beta - m_3\sin\beta)^2 + l_3^2}}, \frac{l_3\sin\beta}{\sqrt{(n_3\cos\beta - m_3\sin\beta)^2 + l_3^2}}, \frac{-l_3\cos\beta}{\sqrt{(n_3\cos\beta - m_3\sin\beta)^2 + l_3^2}}\right) \tag{37}$$

or, in terms of the global axis, we have

$$F_{NX} = \frac{n_3\cos\beta - m_3\sin\beta}{\sqrt{(n_3\cos\beta - m_3\sin\beta)^2 + l_3^2}} F_N \tag{38}$$

$$F_{NY} = \frac{l_3\sin\beta}{\sqrt{(n_3\cos\beta - m_3\sin\beta)^2 + l_3^2}} F_N \tag{39}$$

$$F_{NZ} = \frac{-l_3\cos\beta}{\sqrt{(n_3\cos\beta - m_3\sin\beta)^2 + l_3^2}} F_N \tag{40}$$

C. Boundary Conditions and Constraint Equations

1. Boundary Conditions

Based upon physical considerations, the fiber tip at $s = L$ is moment free, so that the curvature κ, κ' at this point is zero, that is,

$$\kappa(L) = 0 \tag{41a}$$

$$\kappa'(L) = 0 \tag{41b}$$

Figures 2b and 2c are projections of the deformed fiber in the Y_0–Z_0 and X_0–Z_0 plane, respectively. As shown in Fig. 2b, the equilibrium equation along the Z_0 direction can be expressed as

$$\sum F|_{Z_0} = 0 \tag{42}$$

$$T(0) = F_{NZ} + f\sin\beta \tag{43}$$

Similarly, one can enforce equilibrium along the X_0 and Y_0 directions to obtain the following equations:

$$N(0) = F_{NX} - P \tag{44}$$

$$N'(0) = F_{NY} + f\cos\beta \tag{45}$$

In summary, the boundary conditions at $s = 0$ are given by

$$T(0) = F_{NZ} + f\sin\beta \tag{46}$$

$$N(0) = F_{NX} - P \tag{47}$$

$$N'(0) = F_{NY} + f\cos\beta \tag{48}$$

2. Constraint Conditions

As a first constraint condition, one may observed that the coordinate position of the deformed fiber at contact point B [$X(s_1)$, $Y(s_1)$, $Z(s_1)$], namely [reference Eqs. (32–34)]:

$$X(s_1) = \int_0^{s_1} l_3 \, \mathrm{d}s \tag{49a}$$

$$Y(s_1) = \int_0^{s_1} m_3 \, \mathrm{d}s \tag{49b}$$

$$Z(s_1) = \int_0^{s_1} n_3 \, \mathrm{d}s \tag{49c}$$

must lie on the back plate edge ($X_{\xi 2}$, $Y_{\xi 2}$, $Z_{\xi 2}$), which, by inspection of Fig. 2b, is given by

$$X_{\xi_2} = 0 \tag{50}$$

$$Y_{\xi_2} = R_i\sin\theta - (R_s + G^*)\sin\left(\theta + \frac{\xi_2}{(R_s + G^*)}\right) \tag{51}$$

$$Z_{\xi_2} = R_i \cos\theta - (R_s + G^*)\cos\left(\theta + \frac{\xi_2}{(R_s + G^*)}\right) \tag{52}$$

where $R_i = R_s + H^* - \Delta_o^*$. The final form of the constraint equations is thus obtained by combining Eqs. (49a–49c) and (50–52), which yields the following:

$$|X_{\xi_2} - X(s_1)| < \varepsilon \tag{53a}$$

$$|Y_{\xi_2} - Y(s_1)| < \varepsilon \tag{53b}$$

$$|Z_{\xi_2} - Z(s_1)| < \varepsilon \tag{53c}$$

where ε is a prescribed convergence parameter.

Also, the direction cosines (l_3, m_3, n_3) at contact point B $(s = s_1)$ are unknown and must be determined as an integral part of the solution. Because the direction cosines (l_3, m_3, n_3) must satisfy the identity $l_3^2 + m_3^2 + n_3^2 = 1$, only two additional constraint equations are needed to ensure the difference between the initially estimated values $\hat{l}_3$, $\hat{m}_3$ and computed values $\tilde{l}_3$, $\tilde{m}_3$ that were obtained from Eqs. (22–30) will satisfy the convergence criteria, that is,

$$|\hat{l}_3 - \tilde{l}_3| < \varepsilon \tag{54a}$$

$$|\hat{m}_3 - \tilde{m}_3| < \varepsilon \tag{54b}$$

D. Solution Procedure

Governing Eqs. (17–21) are five first order nonlinear differential equations with boundary conditions at $s = L$ [Eqs. (41a) and (41b)] and $s = 0$ [Eqs. (46–48)]. Because a closed-form solution for the governing equations is not feasible, a numerical method (Runga–Kutta) will be applied to solve the current problem. Thus, initial conditions at $s = 0$ for N, N', T, κ, and κ' must be provided. From previous discussion, initial conditions for N, N', T at $s = 0$ were given by Eqs. (46–48). However, the two initial conditions for $\kappa(0)$ and $\kappa'(0)$ are unknown and must be reckoned by an initial estimate. Subsequently, the governing equations are solved using the Runga–Kutta method over the interval $s = 0$ to $s = L$, and the computed values for $\hat{\kappa}(L)$, $\hat{\kappa}'(L)$ are obtained. The difference between $\hat{\kappa}(L)$, $\hat{\kappa}'(L)$ and the known boundary conditions Eq. (41) can be successively reduced to an arbitrarily small value ε by using an iterative solution procedure. Also, notice that an initial guess must be first given for the five unknown variables s_1, $l_3(s_1)$, $m_3(s_1)$, ξ_2 or f, and F_N to compute the initial condition cited in Eqs. (46–48). Subsequently, an iterative convergent solution to the five constraint equations (53a–53c), (54a), and (54b) leads to the unique solution for the five unknown variables.

While solving the governing equations over the interval $s = 0$ to $s = L$, special care must be taken in assessing the solution at $s = s_1$, which corresponds to the location where concentrated force F_N is applied and the internal forces $N(s_1)$, $N'(s_1)$, $T(s_1)$ will undergo an abrupt change due to this load. The following discussion briefly outlines how to compute the internal forces N, N', T at $s = s_1$:

First, according to Eqs. (38–40), one can estimate the components of F_N (F_{NX}, F_{NY}, F_{NZ}) along fixed coordinate axes X_0, Y_0, Z_0. Because each value N, N', T in the governing equations is evaluated with respect to the local coordinate axes, and the cosine directions of the local coordinate axes at $s = s_1$ relative to the fixed axes X_0, Y_0, Z_0 are as indicated in Table 2. Then the components of F_N along local coordinate axes x, y, z at $s = s_1$ (F_{nx}, F_{ny}, F_{nz}) can be expressed as

$$\begin{bmatrix} F_{nx} \\ F_{ny} \\ F_{nz} \end{bmatrix} = \begin{bmatrix} l_1 & m_1 & n_1 \\ l_2 & m_2 & n_2 \\ l_3 & m_3 & n_3 \end{bmatrix} \begin{bmatrix} F_{NX} \\ F_{NY} \\ F_{NZ} \end{bmatrix} \tag{55}$$

Table 2 Cosine directions of local x, y, z axes with respect to fixed X_0, Y_0, Z_0 axes at $s = s_1$

	X_0	Y_0	Z_0
x	$l_1(s_1)$	$m_1(s_1)$	$n_1(s_1)$
y	$l_2(s_1)$	$m_2(s_1)$	$n_2(s_1)$
z	$l_3(s_1)$	$m_3(s_1)$	$n_3(s_1)$

When solving the governing equation along the interval $[0, L]$, one must divide this interval into two subintervals, namely, $0 \le s \le s_1$ and $s_1 \le s \le L$. Upon completing the solution for the first interval, $N(s_1)$, $N'(s_1)$, $T(s_1)$ can be obtained. Before continuing to compute the solution along the interval $s_1 \le s \le L$, the components of the concentrated load F_N along local coordinate system x, y, z axes at $s = s_1$ must be added, that is,

$$N(s_1) = N(s_1) + F_{nx} \tag{56a}$$

$$N'(s_1) = N'(s_1) + F_{ny} \tag{56b}$$

$$T(s_1) = T(s_1) + F_{nz} \tag{56c}$$

Subsequently, the remaining portion of the solution can be obtained such that Eqs. (53) and (54) are satisfied. The trust-region method (Matlab® online help) is employed in the current research for obtaining improved estimated values for $\kappa(0)$, $\kappa'(0)$, s_1, $l_3(s_1)$, $m_3(s_1)$, ξ_2 or f, and F_N. Further details concerning the solution algorithm used in this research can be found in [12].

III. Proposed Approach for Evaluating Hysteresis Phenomenon

In this section, we will examine the hysteresis phenomenon that occurs when the fiber tip is subjected to a transverse load P, which undergoes one complete uploading and downloading cycle as shown in Fig. 4. The load cycle chosen is symmetric, that is, the interval (arbitrary) over which the bristle is uploaded along the linear load history $0 < P < P_{\max}$ is followed by similar downloading over the same interval.

For simplicity, it is assumed that, before the applied cyclic loading, the initial strain energy of the fiber is zero because the fiber is undeformed. At the onset of uploading, the fiber begins to bend and is subjected to both P and f that arises along the back plate edge. Throughout the load history, the fiber is allowed to slide/relocate along the back plate edge as P is varied throughout the load cycle. Thus, both P and f perform work, namely W_{pu} and W_{fu}, respectively, and the strain energy of the fiber increases by the corresponding amount $E_1 = W_{\text{pu}} + W_{\text{fu}}$. While downloading, the fiber may undergo deformation that is different from that of uploading, and, consequently, the work done by f and P can be denoted by W_{pd} and W_{fd}, respectively, and are generally different from W_{pu} and W_{fu}.

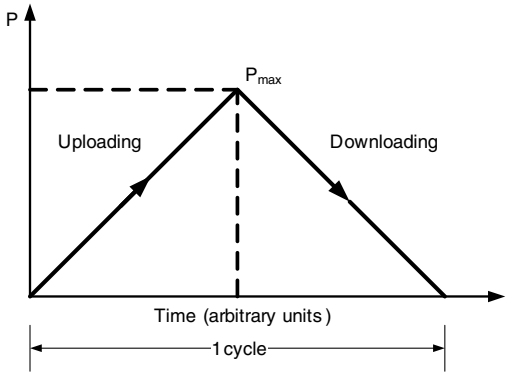

Fig. 4 Hypothetical load history for P.

Thus, the energy recovered during downloading is defined by $E_2 = W_{pd} + W_{fd}$. As the load cycle ends, P and the corresponding friction force is reduced to zero and, therefore, the fiber returns to its initial load-free configuration having a final strain energy content of zero.

According to the relationship between work and energy, the work done by external force must equal ΔE throughout the load cycle, that is,

$$\Delta E = E_1 - E_2 = (W_{fu} + W_{pu}) - (W_{fd} + W_{pd}) \tag{57}$$

where, in the current study, we assume the load is applied quasistatically, that is, kinetic energy is neglected. Because the initial and final strain energy content is zero at the beginning and conclusion of a load cycle, $\Delta E = 0$, and the difference in work done over the load cycle is

$$W_{fu} = W_{fd} = -(W_{pu} - W_{pd}) \tag{58a}$$

$$\Delta W_f = -\Delta W_p \tag{58b}$$

Thus, the differential work ΔW_p done by transverse load P at the conclusion of the load cycle has the same magnitude of differential work ΔW_f done by the friction force over the same load cycle. In the current study, both the direction of the friction force and the displacement (i.e., movement/sliding along the back plate) is along the corner of the back plate itself. As a result, the total work done during uploading and downloading, respectively, is

$$W_{fu} = \int_0^{\xi^*} f \, d\xi_2; \qquad W_{fd} = \int_{\xi^*}^0 f \, d\xi_2 \tag{58c}$$

where ξ^* refers to the maximal displacement along the edge of the back plate. Because Eq. (58c) merely represents the area under the uploading/downloading traversals, respectively, it is apparent that the *hysteresis* directly corresponds to the disparity between uploading and downloading paths, that is, the net area that encloses the uploading/downloading paths exactly corresponds to ΔW_f. In conclusion, this provides a basis for evaluating the hysteresis H associated with one complete load cycle as follows:

$$H = \Delta W_f = \oint f \, d\xi_2 = W_{f_u} - W_{f_d} \tag{58d}$$

IV. Numerical Results and Discussion

A. Validation of Model

In this section, the correctness of the present numerical results is validated by a direct comparison with a closed-form solution reported by Howell and Lattimer [8]. Figure 5 illustrates the mechanics problem proposed in [8], whereby a single fiber is clamped at one end to a flat surface oriented in the horizontal plane. One may observe that the free end of the bristle hangs off of the table edge. The concentrated load P is lumped at the free end of the fiber and represents the total force exerted by oncoming flow of gas through the interface of the rotor/back plate region. In [8], deformation of the fiber is assumed to satisfy small deformation theory, and displacements are examined in both the x and y directions. The closed-form solution for dimensionless displacement along the x and y directions, $\bar{u} = u/l$ and $\bar{v} = v/l$, respectively, are written in terms of the current paper nomenclature as follows:

$$\bar{u} = \begin{cases} \frac{1}{48}\tan\theta[\bar{z}^2(1-\bar{L})(3-\bar{L})(\bar{z}-3\bar{L})\bar{P}^2] & 0 \le \bar{z} \le \bar{L} \\ \frac{1}{48}\tan\theta[\bar{L}^2(3-\bar{L})(1-\bar{L})(\bar{L}-3\bar{z})\bar{P}^2] & \bar{L} \le \bar{z} \le 1 \end{cases} \tag{59}$$

$$\bar{v} = \begin{cases} \frac{1}{4\bar{L}}(\bar{L}-1)(\bar{z}-\bar{L})\bar{z}^2\bar{P} & 0 \le \bar{z} \le \bar{L} \\ \frac{1}{12}(\bar{L}^3 - 3\bar{L}^2 + 2 + 3(\bar{L}-1)(2-\bar{L})\bar{z} + 2(\bar{z}-1)^3\bar{P} & \bar{L} \le \bar{z} \le 1 \end{cases} \tag{60}$$

where $\bar{P} = PL^2/EI$ is the nondimensional axial load, and $\bar{z} = z/L$ is the nondimensional coordinate along the z axis, and $\bar{L} = b/L$ is nondimensional distance along the fiber length where contact is made along the edge of the back plate.

Thus, the corresponding dimensionless displacements $\bar{u}$, $\bar{v}$ at the fiber end ($\bar{z} = 1$) for various $\bar{P}$ can be derived from the above equations, and are given by the following:

$$\bar{u}|_{\bar{z}=1} = \frac{1}{48}\tan\theta\bar{L}^2(1-\bar{L})(3-\bar{L})(\bar{L}-3)\bar{P}^2 \tag{61a}$$

$$\bar{v}|_{\bar{z}=1} = \frac{1}{12}(\bar{L}^3 - 3\bar{L}^2 + 2 + 3[\bar{L}-1)(2-\bar{L})]\bar{P} \tag{61b}$$

Figure 6 shows a comparison of the results from [8] and the current general bending theory for $\theta = 0$, $\mu = 0$, $l = 0.286$ in., $I = 3.0171 \times 10^{-12}$ in.^{4}, $E = 30 \times 10^6$ psi, where the dotted line shows the results from Eqs. (59) and (60), and the solid line shows the numerical results from general bending theory. For the current case ($\theta = 0$), it is apparent that the fiber only deforms in the x–z plane, and, consequently, the nondimensional displacement $\bar{u}$ along the x direction is zero. Thus, both linear beam theory and general bending theory have the same results for the $\bar{u}$ displacement. As for the $\bar{v}$ displacement, when $\bar{P}$ reaches the point $\bar{P} = 5.346$ (shown as a vertical line), the slope at the end of the cantilever beam is equal to 0.1 rad, which is often taken as the limit of applicability for linear beam theory. Accordingly, the difference between these two results is small, and linear beam theory is regarded as valid to predict the bristle deformation within this load range [13].

However, as $\bar{P}$ continuously increases, the difference between these two different solutions increases. For example, at $\bar{P} = 10$, the difference between these two solutions is approximately 10%. Also notice, under the same load $\bar{P}$, the nondimensional displacement $\bar{v}$ from general beam theory is always less than that of linear beam theory, which means the current bending model is stiffer than the model proposed in [8]. To account for this behavior, the current

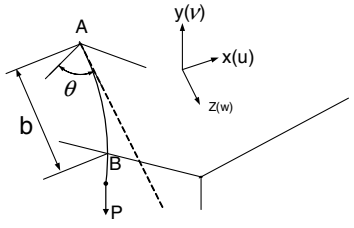

Fig. 5 Depiction of bristle bending model used by Howell and Lattimer [8].

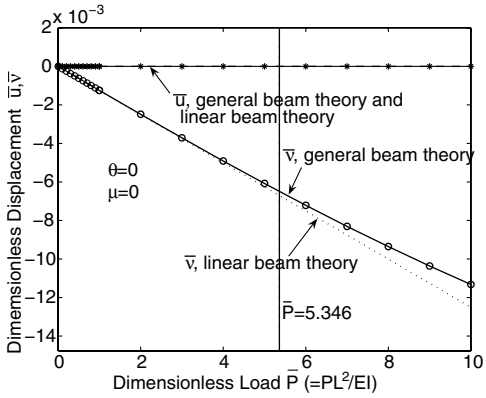

Fig. 6 Comparison of nondimensional displacement at fiber tip under the action of dimensionless force based upon general beam theory and linear beam theory.

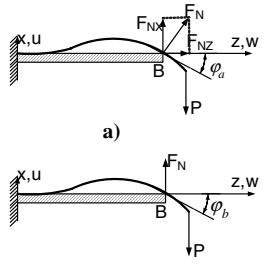

Fig. 7 Interpretation/explanation of different force system directions for F_N, using general beam theory and linear beam theory (results shown are for bristle with lay angle $\theta = 0$).

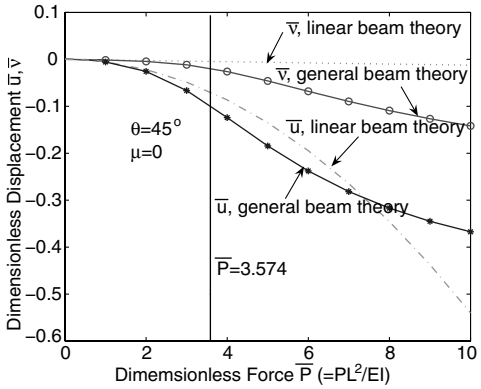

Fig. 8 Comparison of nondimensional displacement at fiber tip under the action of dimensionless force for general beam theory and linear beam theory.

problem is further illustrated in Fig. 7, whereby one may observe that for the current model, the reaction force F_N at the back plate edge is reckoned to be perpendicular to the local slope of the elastica at contact point B. As a result, there exists both a force component F_{NX} along the (transverse) x direction and a force component F_{NZ} along the z direction, which resists transverse fiber deformation. In contrast, for linear beam theory, the reaction force F_{NZ} is assumed parallel to P, that is, in the transverse direction only, and therefore, the "apparent" stiffness of the fiber is less than that obtained in the present result. This is also consistent with the difference in slopes obtained for the two different solutions that is, $\phi_a < \phi_b$, as depicted in Fig. 7.

Figure 8 compares the two different solutions for $\mu = 0$, $\theta = 45$ deg, $l = 0.286$ in., $I = 3.0171 \times 10^{-12}$ in.^{4}, $E = 30 \times 10^6$ psi. One may observe that when $\theta \neq 0$, the fiber deformation occurs in both the x and y direction. The vertical line $\bar{P} = 3.574$ shows the position where the slope at the fiber reaches 0.1 rad for the dimensionless displacement $\bar{u}$. Here, a discrepancy of nearly 30% is observed for the two different solutions. Moreover, linear beam theory indicates that the displacement $\bar{u}(\bar{L})$ increases with the square of $\bar{P}$ [refer to Eq. (59)], whereas the present model forecasts that a more complex behavior of the bristle tip displacement $\bar{u}(\bar{L})$ occurs at higher load levels.

B. Hysteresis Case Studies

In this section, the model developed herein for out-of-plane bending of a brush seal bristle is applied to a fiber whose tip is subjected to the axial load P. Specifically, the normal and frictional contact force along the interface of the bristle and back plate edge is computed. Subsequently, the friction force f is used as a basis for computing the work done, as the side of the bristle slides along the curved edge of the back plate. As noted in Sec. III, the corresponding hysteresis can be readily computed for various frictional contact conditions of interest. In the current study, we explore two different frictional conditions, namely, $\mu_s = \mu_k$ and $\mu_s > \mu_k$, in conjunction with the load cycle shown in Fig. 4. The load cycle chosen is symmetric, that is, linearly uploading over the excursion $0 \leq P \leq P_{\max}$ is followed by similar downloading over the same interval.

Case 1. $\mu_s = \mu_k$

Results are shown in Fig. 9a for the special case $\mu_s = \mu_k = \mu$ for several different friction coefficients, that is, $\mu = 0.0, 0.01, 0.1, 0.21, 0.3, 0.32, 0.35$, and 0.4. To facilitate this illustration, the upload portion of the load cycle for $\mu_s = \mu_k = 0.21$ has been depicted by the segment of the curve a–b–c. Similarly, the download portion of the load cycle is represented by the segment of the curve c–d–a, thereby completing the cycle. Throughout the excursion, each data point (open circle) represents an incremental change of the applied axial force. One may observe that for the chosen load cycle, the uploading and downloading paths have a similar history. For example, the selection of friction coefficient $\mu = 0.21$ leads to an initial resistance (segment a–b), and is followed by a smooth sliding motion of the bristle side along the back plate edge (segment b–c) up to point c, whereupon maximum axial force $P_{\max}$ is reached. Similarly, downloading is accompanied by an initial resistance of the fiber to return to its original configuration (segment c–d). However, upon reaching a directionally reversed frictional force of sufficient magnitude (i.e., at point d), the bristle undergoes smooth sliding motion as it returns to the initial load-free equilibrium position (segment d–a). For the limiting case of $\mu = 0.0$, no frictional load exists, and the expected result is shown in Fig. 9a, whereby, uploading and downloading yields the same path.

As previously explained, hysteresis is computed on the basis of the net area generated by each closed path having the constant friction

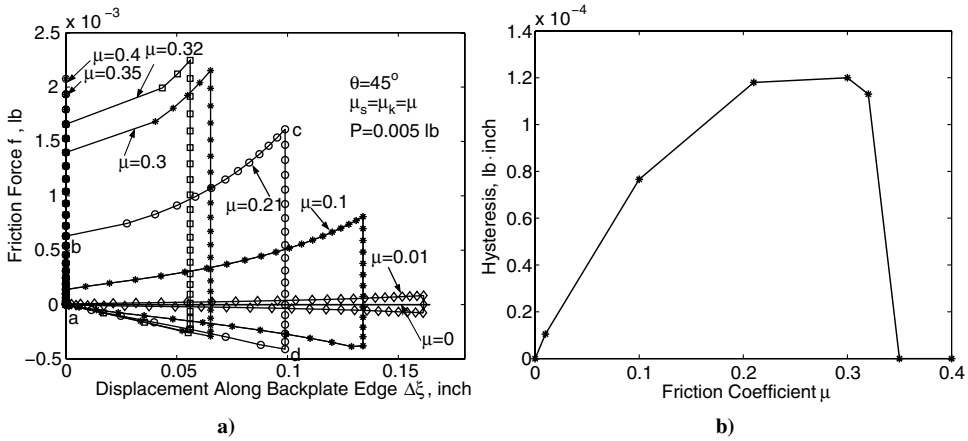

a) b)

Fig. 9 a) Response curve f–$\Delta\xi$ under axial load cycle $P = 0 \rightarrow 0.005 \rightarrow 0$ lb for a bristle with lay angle $\theta = 45$ deg; b) enclosed area (hysteresis) for various μ.

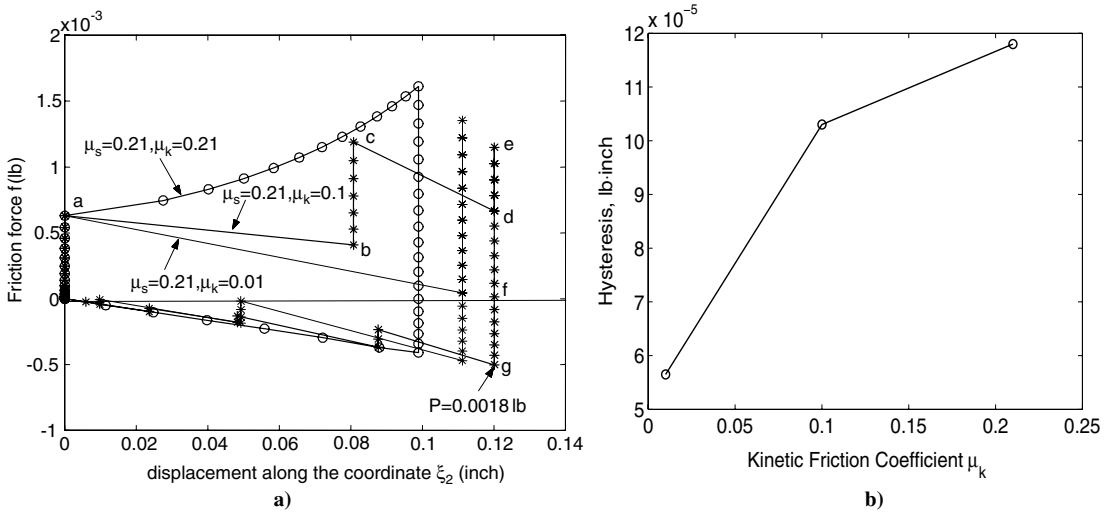

a) b)

Fig. 10 a) Response curve f–$\Delta\xi$ under axial load cycle $P = 0 \rightarrow 0.005 \rightarrow 0$ lb for a bristle with lay angle $\theta = 45$ deg for $\mu_s \geq \mu_k$; b) the enclosed area (hysteresis H).

coefficient shown in Fig. 9a. This net area is plotted in Fig. 9b for each friction coefficients and demonstrates that the magnitude of hysteresis regularly increases as the friction coefficient increases. However, a maxima for the hysteresis is reached at approximately $\mu = 0.3$, whereupon the energy loss declines as μ is further increased. For the chosen values of friction coefficient greater than 0.32, no hysteresis is recorded. This is consistent with the expected result, because for a sufficiently large friction coefficient, no movement of the fiber is allowed along the edge of the back plate, that is, the bristle is "pinned" at its equilibrium position. Although the above study indicates that no hysteresis is detected for $\mu_s = \mu_k \geq 0.35$, this result cannot be construed as beneficial. That is, because the bristle remains pinned throughout the load cycle, one may expect that such larger values of friction coefficient can lead to increased stiffening of the bristle/seal system.

Case 2. $\mu_s \geq \mu_k$

In Fig. 10, the results are shown for $\mu_s = 0.21$ and $\mu_k = 0.01, 0.1$, and 0.21, respectively. An obvious stick-slip phenomenon is observed for $\mu_s > \mu_k$. For example, for $\mu_s = 0.21$ and $\mu_k = 0.01$, as P is applied incrementally, the static friction force begins to accumulate, and the fiber sticks to its original position at the back plate. However, upon reaching a maximum static friction force of $F_{\text{sa}} = 6 \times 10^{-4}$ lb (i.e., point a), the fiber moves (slips) toward a new equilibrium position at point b. Subsequently, as P is continually increased, the static friction force will again build up at its current equilibrium position, where the fiber remains pinned (i.e., path b–c). As the normal load P is further increased, the static friction force reaches a new maximum value $F_{\text{sc}} = 12 \times 10^{-4}$ lb (i.e., point c), and the fiber slides along the back plate to achieve a new equilibrium position, that is, to point d. To complete the uploading portion of the load cycle, the normal force P is further increased, however, the fiber remains locked in position (i.e., path d–e), even as the friction force continues to increase. While unloading P, the fiber remains at its current position along the back plate, and the friction force rapidly decreases. Upon declining to the point f, whereby the friction force is zero, the friction force subsequently changes sign, that is, the direction of friction force has been reversed. As the axial load is further decreased to the value of $P = 0.0018$ lb, the fiber begins to retract along the edge of the back plate. Similarly, the stick-slip phenomenon that was identified during uploading also appears during the downloading process. Finally, when $P = 0$, closure of the hysteresis loop occurs, and the enclosed area of the hysteresis path can be computed. It is of interest to compare the hysteresis associated with various kinetic friction coefficients μ_k while keeping the static friction coefficient μ_s constant. Thus, Fig. 10b records the hysteresis for each friction condition shown in Fig. 10, whereby it is observed that the energy loss is the greatest when the static and kinetic coefficients of friction are identical (i.e., $\mu_s = \mu_k = 0.21$). This indicates that a reduction of the kinetic coefficient of friction leads to a reduction of hysteresis.

V. Conclusions

In this research, a three-dimensional model has been developed to examine large displacement of a brush seal bristle that resides along the back plate and is subjected to a concentrated transverse (axial) load at the fiber tip. The numerical solutions obtained herein have been validated by a direct comparison with the results reported by Howell and Lattimer [8], which used linear beam theory. Based upon the results reported in this paper, the following conclusions are surmised:

1) As one may expect, linear beam theory is adequate for computing bristle deformation at lower load levels. However, at elevated load levels, general beam theory must be applied to obtain accurate deformation of the bristle.

2) Under the action of P, the specification of a nonzero θ gives rise to three-dimensional deformation, that is, the bristle not only bends in the direction of P, but also slips along the edge of back plate.

3) The hysteresis phenomenon can be modeled as an energy loss during an axial flow-induced load cycle, which is the same as the work done by the frictional force generated along the interface of the bristle and back plate edge.

4) For $\mu_s = \mu_k = \mu$ the magnitude of hysteresis increases as the friction coefficient is increased. A further increase of the friction coefficient, however, leads to an upper bound for the hysteresis. At this point, any additional increase in μ leads a declining loss of energy, because bristle slippage is restricted. Finally, upon reaching the critical value of friction coefficient $\mu = \mu_{\text{cr}}$, no movement along the back plate edge is allowed and the side of the bristle remains pinned for all $\mu > \mu_{\text{cr}}$.

5) For the case of $\mu_s > \mu_k$ an obvious stick-slip phenomenon is observed. Moreover, results show that as the kinetic friction coefficient is successively reduced, the magnitude of hysteresis $|H|$ is likewise reduced.

References

[1] Bayley, F. J., and Long, C. A., "A Combined Experimental and Theoretical Study of Flow and Pressure Distributions in a Brush Seal," *Journal of Engineering for Gas Turbines and Power*, Vol. 115, No. 2, 1993, pp. 404–410.

[2] Wood, P. E., "Investigation of Contact Forces, Flow, Pressure, Hysteresis and Frictional Effects in Brush Seals," Ph.D. Dissertation, University of Oxford, 1998.

[3] Chen, L. H., Wood, P. E., Jones, T. V., and Chew, J. W., "An Iterative

CFD and Mechanical Brush Seal Model and Comparison with Experimental Results," *Journal of Engineering for Gas Turbines and Power*, Vol. 121, No. 4, 1999, pp. 656–662.

[4] Zhao, H., and Stango, R. J., "Effect of Flow-Induced Radial Load on Brush Seal/Rotor Contact Mechanics," *Journal of Tribology*, Vol. 126, No. 1, 2004, pp. 208–215.

[5] Chupp, R. E., and Dowler, C. A., "Performance Characteristics of Brush Seals for Limited Life Engines," *Journal of Engineering for Gas Turbines and Power*, Vol. 155, No. 2, 1993, pp. 390–396.

[6] Basu, P., Datta, A., Loewenthal, R., and Short, J., "Hysteresis and Bristle Stiffening Effects in Brush Seals," *Journal of Propulsion and Power*, Vol. 10, No. 4, 1994, pp. 569–575.

[7] Aksit, M. F., "A Computational Study of Brush Seal Contact Loads with Friction," Ph.D. Dissertation, Rensselaer Polytechnic Institute, 1998.

[8] Howell, P. D., and Lattimer, T. R. B., "Modeling Bristle Bending in Brush Seals," *Mathematical Engineering in Industry*, Vol. 7, No. 3, 1999, pp. 349–359.

[9] Zhao, H., and Stango. R. J., "Role of Distributed Interbristle Friction Force on Brush Seal Hysteresis," *2004 Seals/Secondary Air System Workshop*, NASA Glen Research Center, Cleveland, OH, Nov. 2004.

[10] Chew, J. W., Lapworth, B. L., and Millener, P. J., "Mathematical Modeling of Brush Seals," *International Journal of Heat and Fluid Flow*, Vol. 16, No. 6, 1995, pp. 493–500.

[11] Love, A. E. H., *A Treatise on the Mathematical Theory of Elasticity*, 4th ed., Dover Publications, New York, 1944, Chaps. 18 and 19.

[12] Zhao, H., "Modeling, Analysis and Design Considerations for Brush Seals Used in Turbomachinery Applications," Ph.D. Dissertation, Marquette University, 2005.

[13] Budynas, R. G., *Advanced Strength and Applied Elasticity*, 2nd ed., McGraw–Hill, New York, 1999, pp. 152–156.

T. Shih
Associate Editor